Contents lists available at SciVerse ScienceDirect

Applied Catalysis B: Environmental

Quantum yield with platinum modified TiO$_2$ photocatalyst for hydrogen production

Salvador Escobedo Salas [a], Benito Serrano Rosales [b], Hugo de Lasa [a,*]

[a] Western University, Faculty of Engineering, Chemical Reactor Engineering Centre (CREC), London, ON, Canada
[b] Universidad Autónoma de Zacatecas, Facultad de Ciencias Químicas, Zacatecas, Zacatecas, Mexico

ARTICLE INFO

ABSTRACT

The present study reports quantum yields for hydrogen production using a Pt modified titanium dioxide (DP25) photocatalyst in a slurry medium, under near-UV irradiation. The photocatalyst was prepared using the incipient wetness impregnation method. The modified photocatalyst exhibited a reduced energy band of 2.73 eV upon Pt addition. Experiments were performed in a Photo CREC Water II Reactor. This unit allows the establishment of macroscopic radiation balances. These irradiation balances showed a maximum LVREA (local volumetric rate of energy absorption) of 0.15 g/L. Regarding hydrogen formation via H• radicals, the addition of a 2 vol.% ethanol scavenger allowed achieving significant amounts of hydrogen free of oxygen. It was noticed that the rate of hydrogen formation in the presence of ethanol is a function of the pH of the water solution. It was also observed that the calculated 7.8% quantum efficiency showed good degree of photon utilization and confirmed the value of the Pt modified TiO$_2$ photocatalyst and Photo CREC Water II Unit set up for hydrogen production, via water splitting.

1. Introduction

Energy band engineered materials such as modified TiO$_2$ photocatalysts display promising properties for environmental applications including hydrogen production via water splitting [1–5]. These materials appear to contribute to hydrogen formation. This occurs via the modification of both the energy band gap and the formation of a Schottky barrier which retards the charge recombination at the TiO$_2$ particle outer surface. This phenomenon appears to promote the efficient separation of holes and electron charges under UV-light irradiation. Hence, photocatalytic activity can be enhanced using TiO$_2$ dopants, promoting H• radical formation and hydrogen production [6–10].

In 1972, Fujishima and Honda were the first to report photoassisted water electrolysis using the rutile form of TiO$_2$ as the photoanode of a photoelectric cell [11]. The development of novel semiconductors (photocatalysts) has increased in recent years. New semiconductors such as TiO$_2$ combined with either tantalate compounds [1,12] or noble metals [2,13–17] under UV or visible light have gained importance for hydrogen production. These photocatalysts have been studied in different photocell configurations under different conditions. It has been noticed that in the absence of both a sacrificial agent and a noble metal, the e$^-$/h$^+$ recombination on the semiconductor surfaces can occurs quickly. Therefore, the efficiency of photocatalytic hydrogen production is very low.

To achieve higher efficiencies however, different "sacrificial agents" have been proposed such as alcohols, carbohydrates, hydrocarbons and organic pollutants. These materials, so-called "hole scavengers" can react irreversibly with the holes (h$^+$) on the semiconductor outer surfaces. Nevertheless, to be able to use them in practice, electron donors must be cheap and easily accessible [2,3]. Furthermore, sacrificial agents should not be derived from fossil fuels. Sacrificial agents should be a renewable resource or derived from them such as ethanol [18–20]. This will make hydrogen production a sustainable process. Otherwise, the main environmental advantage of producing hydrogen via water splitting and solar energy will be loss or partially lost.

In this respect, it is envisioned that a good and low cost "sacrificial agent" can be ethanol in low concentrations (1–2 vol.%) [3]. Low ethanol concentrations can be obtained from the natural fermentation of glucose, fructose, sucrose and even agricultural waste [21–23].

During photocatalytic oxidation, the photocatalyst absorbs UV light, which excites electrons from the valence band into the conduction band. The resulting electron (e$^-$)/hole (h$^+$) pairs can then migrate to the surface of the semiconductor and initiate redox reactions with adsorbed organics and protons [1,2,4,5,13,18,24,25].

Regarding solar light, near-UV light in the 340–388 nm wavelength range corresponds to 4–5% of the complete solar

* Corresponding author. Tel.: +1 519 661 2144.
E-mail address: hdelasa@eng.uwo.ca (H. de Lasa).

Nomenclature

a_v	catalyst transference area (cm^2/cm^3)
C_2H_4O	acetaldehyde
c	speed of light (3.0×10^8 m/s)
C	photocatalyst loading (g/l)
d_p	porous diameter (cm)
e^-	electron
h^+	hole
h	Planck's constant (6.63×10^{-34} J/s)
$E(\lambda)$	energy of a photon at a given wavelength (J)
E_{bg}	energy band gap (eV)
E_{av}	average energy of a photon (kJ/mol photon)
eV	electron volts
H_2PtCl_6	chloroplatinic acid
$H^\bullet$	hydrogen radical dot
$[H^+]$	protons (μmole/cm^3)
$I(\lambda)$	intensity of light (W/cm^2)
I_A	X-ray anatase peak intensity
I_R	X-ray rutile peak intensity
k_f	mass transfer coefficient (cm/s)
k_r	reaction transfer coefficient
L	length of the lamp (cm)
M^0	basal state metal
N_i	number of i molecules produce
P_0	rate of photons emitted by the BLB lamp (einsteins/s)
P_a	rate of absorbed photons (einstein/s)
P_{a-wall}	rate of photons absorbed by the inner Pyrex glass (einstein/s)
P_{bs}	rate of backscattered photons exiting the system (einstein/s)
P_{fs}	rate of forward-scattered radiation (einstein/s)
P_i	rate of photons reaching the reactor inner surface (einstein/s)
P_{ns}	rate of transmitted nonscattered radiation (einstein/s)
P_t	rate of transmitted photons (einstein/s)
Pt	platinum
$q(\theta,z,\lambda,t)$	net radiative flux over the lamp emission spectrum ($\mu W/cm^2$)
r	radial coordinate
Redox	reduction oxidation reactions
t	time (h)
TiO_2	titanium dioxide
V	reactor volume
W	weight (g)
wt%	weight percent (% m/m)
x	intensity weight fraction (%)
z	Cartesian coordinate (m)

Greek symbols

γ	stoichiometric coefficient of hydrogen
θ	diffraction angle, also scattering angular angle ($\circ$)
λ	wavelength (nm)
ρ	density (g/cm^3)
τ	stoichiometric coefficient of acetic acid
φ	efficient quantum yield (%)

Acronyms

BLB	black light blue lamp
BET	Brunauer–Emmett–Teller surface area method
CB	conduction band
DP25	TiO_2 Degussa P25

EtOH	ethanol
FIB	focused ion beam
ID	internal diameter
LTU	lamp testing unit
LVREA	local volumetric rate of energy absorption
NTP	normal temperature pressure
PCW-II	Photo CREC Water II reactor
PEC	photo-electric-cell
QY	quantum yield
RID	refractive index detector
UV	ultra violet
VIS	visible
VB	valence band

Subscripts

ads	adsorbed
av	average
bg	band gap
cat	photocatalyst
gt	gas tank
i	any number of reaction path
int	intersection
L	liquid
max	maximum
min	minimum
theor	theoric
T	total

Superscripts

0	basal state
*	star or excited state

irradiation spectrum [18,24,25]. Thus, the application of the DP25 photocatalyst with solar light is limited. Nevertheless, platinum can retard both charge recombination (e^-/h^+) and serve as a temporary electron reservoir. The accumulated electrons on platinum can eventually react with water or protons forming $H^\bullet$ radicals [6,7,19,21]. As a result, the electron band gap (E_{bg}) and the photocatalytic activity for hydrogen generation can be improved [8,9,20].

Experiments in hydrogen formation via water splitting were performed in this study using a Photo CREC Water II Reactor with a specially designed H_2 collector tank. This study also took advantage of a modified semiconductor material (Pt/TiO_2) with a conveniently reduced band gap and 2 vol.% ethanol (EtOH) as a h^+ scavenger. Experiments with near-UV light and Pt modified TiO_2 were performed under the special condition of having "all" irradiated photons with photon energies superseding the band gap of the semiconductor. This approach also allows establishing quantum yields for hydrogen production using the entire irradiation beam spectrum from the near UV lamp.

2. Experimental

2.1. Preparation of Pt/TiO2 photocatalyst

DP25 Titanium dioxide (TiO_2) from Evonik Degussa Co. was used as semiconductor "support" to prepare the modified photocatalyst of the present study [14,26,27]. Platinum on DP25 photocatalysts was prepared using incipient wetness impregnation achieving 0.0616, 0.103 and 0.23 and 1 wt% loadings [28,51].

DP25 was dried at 140 °C for 6 h before impregnation to desorb water and some other species potentially present on the TiO_2 particles. A 99.9 wt% $H_2PtCl_6 \cdot xH_2O$ reagent from Sigma–Aldrich Co. was

dissolved in distillate water to produce the different impregnating Pt solution concentrations.

The first Pt impregnation step was carried out at vacuum conditions with continuous mixing of the TiO_2 support. A 4 ml of the precursor solution was employed. This solution was prepared with different precursor concentrations as required by the desired platinum loading to be used. A 2 ml aliquot of this precursor solution was added to 5 g of TiO_2 in a drop-by-drop manner. Once the liquid addition was complete, the impregnating solution and the TiO_2 were left in contact with each other for 10 min. The wet photocatalyst was heated up to 140 °C during 30 min using a 4.6 °C/min temperature ramp. Furthermore, the photocatalyst was left for another 2 h at 140 °C. This allowed water evaporation from the TiO_2 support leaving the H_2PtCl_6 phase on the photocatalyst outer surface. The dried photocatalyst cake was crushed in a mortar until the resulting particles were fine enough, and reached an acceptable size.

Following this, a second impregnation step was carried out using a 2 ml of the remaining precursor solution and contacting it with 5 g of the TiO_2 already impregnated one time. The twice impregnated photocatalyst was now dried at 160 °C for 3 h following a 5.3 °C/min temperature ramp. The resulting photocatalyst cake was crushed and later grinded in a mortar. The finely grinded particles which were obtained displayed a particle size distribution which is shown later in Fig. 6.

Furthermore, the resulting particles were heated up to 450 °C during 1 h using a 7.5 °C/min temperature ramp and were left in the oven at 450 °C for another 3 h. The 450 °C temperature was selected to ensure that chlorine was fully removed [14,26–28].

Finally, the photocatalyst was placed in a flow reactor unit under a 1 cm^3/s of Ar/H_2 (g) (90/10%, Praxair) reducing mixture. Reduction steps involved the following: (a) a 6.6 °C/min temperature increase during 1 h and (b) once 400 °C reached, this temperature was kept here for another 3 h.

In summary, and using the preparation procedure described in this section, platinum (M^0) particles were formed on the TiO_2 particle outer surfaces.

2.2. Photocatalyst characterization

Prepared photocatalysts were characterized using: (a) specific surface area, (b) chemisorption, (c) X-ray diffraction, (d) particle size distribution, (e) X-ray fluorescence, (f) UV–VIS–NIR spectra and (g) images and elemental mapping.

The specific surface areas of all prepared photocatalysts were determined using a BET surface area analyzer (Micrometrics, ASAP 2010) and using nitrogen adsorption. A photocatalyst sample was dried and degassed in a sample tube at 300 °C for at least 3 h before adsorption. The results were assessed by using the Autosorb ASAP 2010 software, Version 5.02.

Moreover, the active metallic particle size (crystallite size) and metal dispersion were calculated by pulse chemisorption analysis (Micrometrics, AutoChem II 2920 V 4.00). The crystalline phases of the photocatalysts were investigated using a X-ray diffractometer RIGAKU Ultima IV (Multi-Purpose Diffractometer). This instrument features a 3-kW X-ray beam with a high-precision 2θ wide-angle horizontal goniometer as well as "cross beam optics". The particle size distribution of the prepared photocatalyst was measured by using a Malvern Zetasizer Nano-Series.

The elemental composition analysis of the photocatalyst was established by X-ray Fluorescence (Philips PW-1480 Wavelength Dispersive Spectrometer) and quantified by utilizing the Iniquant Software. The band gap of the photocatalyst was determined by employing an UV–VIS–NIR Spectrophotometer (UV-3600 Shimadzu).
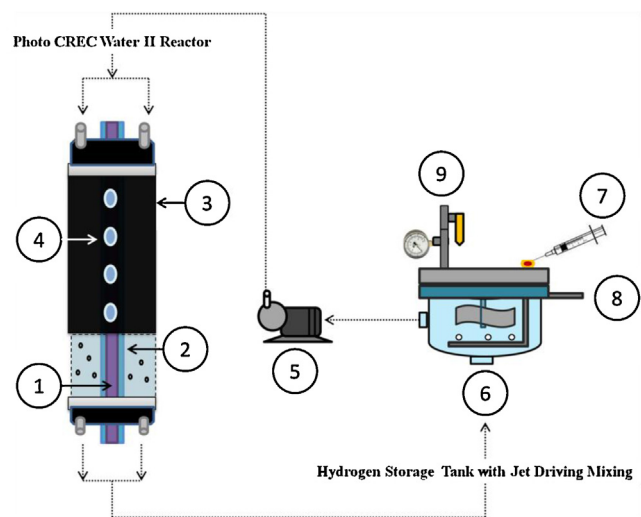

Fig. 1. Schematic diagram of the Photo CREC Water II with H_2 mixing tank: (1) BLB lamp, (2) Pyrex glass tube, (3) UV-opaque polyethylene cylinder, (4) fused-silica windows, (5) centrifugal pump, (6) H_2 storing/mixing tank, (7) gas sampling port, (8) purging gas injector and (9) draining gas valve.

Images and elemental mapping of the photocatalyst were performed using SEM/EDX (LEO/Zeiss 1540XB FIB/SEM). The ion beam column was utilized for in situ sectioning of samples which were imaged by SEM. The system was fitted with an Oxford Instruments X-ray system allowing for elemental mapping and analysis of the selected sample milled sections. In this way, samples could be monitored in real time at high resolution with an electron column (selective etching can be achieved with sub-100 nm resolution).

2.3. Lamp characterization

The lamp testing unit (LTU) developed by Serrano and de Lasa [52] was used to calibrate the BLB lamp. The LTU Unit consists of a UV-opaque chamber, a lamp holder and a spectrometric sensor holder rail. Irradiation spectrum measurements can be performed with the sensor cell facing the lamp. The sensor is displaced along a rail which is located at a fixed distance from the lamp axis [29].

2.4. Photocatalytic reactor

A novel Photo CREC Water II Reactor was used in the present study (Fig. 1). This modified Photo CREC Water II Reactor operates as a "well mixed" batch unit. This unit includes major changes required for hydrogen production, such as a self-driven mixing stirrer and a hydrogen storage tank.

The modified Photo CREC Water II Reactor for hydrogen production also includes two concentric tubes to provide a radial and axial symmetric irradiation field. The first tube is a transparent inner cylinder of Pyrex glass, that was used due to the fact it only absorbs 5% of the emitted near UV-Light (It has a good near UV-Light transmission properties) and has a low cost. A Black Light Blue Lamp of 15 W is placed inside this glass tube and has an emission range of 340–410 nm. The second and outer tube is made out of UV opaque polyethylene to minimize radiation reflection. Moreover, this outer reactor tube facilitates radiometric, spectro-radiometric measurements and performance of macroscopic energy balances for energy efficiency calculations. In addition, it provides a free-flowing photocatalyst suspension in the concentric annular channel.

Fig. 1 reports a schematic diagram of Photo CREC Water II Reactor and accessories. This figure shows the overall unit configuration: a sealed stirred tank chamber connected in series with a tubular photocatalytic reactor. The Photo CREC Water II Reactor

Table 1
Photo CREC Water II H_2 mixing/storing tank dimensions and characteristics.

Component	Parameter	Value
1. Black Light Blue Lamp (BLB USHIO)	Length (cm)	41.2
	Radius (cm)	1.75
	Nominal input power (W)	15
	Output power (W)	4
	Emission range (nm)	340–410
	Emission rate (einsteins/s)	1.14×10^{-5}
	Efficiency (%η)	25
	Average energy (kJ/mol photon)	324
2. Inner cylinder (Pyrex glass)	Length (cm)	61
	Internal radius (cm)	1.505
	External radius (cm)	1.75
	Thickness (cm)	0.22
3. Annular reactor	Height (cm)	45
	Internal radius (cm)	1.75
	External radius (cm)	4.5
4. Windows (fused silica)	Diameter (cm)	1
	Thickness (cm)	0.312
5. Pump (Little Giant Co.)	Voltage	115
	Amperes	1.7
	Hertz	60
	Horse power	1/20
	RPM	300
6. H_2 mixing/storing tank	Internal radius (cm)	22.8
	External radius (cm)	31
	Height (cm)	21
*Internal tank impeller	Diameter (cm)	4.5
	Height (cm)	16.5
**Acrylic lid with integrated septum	Radius (cm)	15.5
	Thickness (cm)	1.5

Fig. 2. Near-UV irradiation spectrum of a USHIO BLB lamp in the Photo CREC Water II Reactor. (a) The shaded area describes the region of the spectrum with a wavelength smaller than 388 nm. (b) The cleared area describes the region of the spectrum with a wavelength larger than 388 nm and smaller than 455 nm.

includes the additional following components: (i) a BLB lamp, (ii) a Pyrex glass tube, (iii) a UV-opaque polyethylene cylinder, (iv) fused-silica windows, (v) a centrifugal pump, (vi) a H_2 storing/mixing tank, (vii) a gas sampling port, (vii) a purging gas injector and (viii) a draining gas valve. Dimensions of the main components of Photo CREC Water II as adapted for hydrogen production are given in Table 1.

Regarding the sealed well mixed tank, it was designed and equipped to accomplish the following: (i) provide jet driven mixing for TiO$_2$–water slurry free of sealing issues and hydrogen losses, (ii) take aliquot samples (gas and liquid) allowing measurements of organic scavengers and hydrogen, (iii) add the photocatalyst (Pt/TiO$_2$), (iv) store H_2, (v) feed inert gases (N_2 or Ar) as needed, (vi) measure the pH and (vii) monitor the temperature. A centrifugal pump circulates the fluid throughout the system and is used to modify the flow rate.

Prior to the experiments, the photocatalyst was sonicated for a 10 min period to ensure good particle distribution in the slurry solution before being added to the water/ethanol solution in the storage tank.

2.5. Analytical techniques

The GC, a unit manufactured by Shimadzu GC-2010 equipped with a Grace Hayesep D packed column 100/120 mesh (9.1 m × 2 mm × 2 μm nominal) was used to separate H_2, CO, CO_2, CH_4, C_2H_4O from O_2 and N_2 (air). Furthermore, this GC has TCD and FID detectors as required for the quantification of various species. The Ar carrier gas has high purity (Praxair 99.999%). The use of argon as a carrier allows increasing the sensitivity of the detector toward H_2. The GC was interfaced with a desktop that enables the analysis of the injected samples. The samples of 0.8 ml were taken manually (Hamilton CO. gastight valve-syringe of 1 ml)
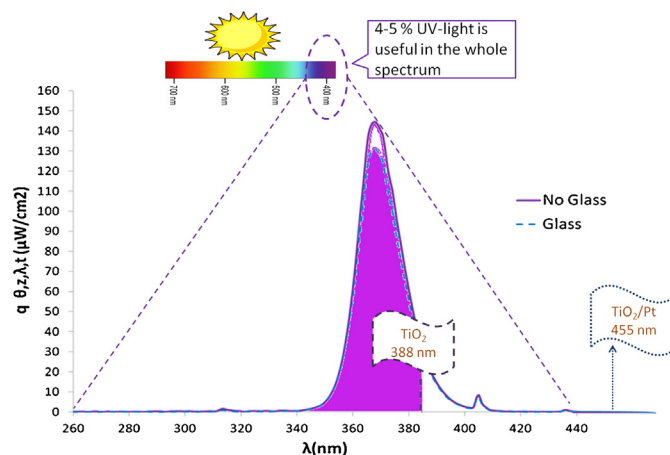
from the PCW-II mixing/storing H_2 tank at set times. They were then injected in a GC port for analysis. The calibration of the GC TCD detectors was made using several mixtures of known gas concentrations.

The UFLC-Shimadzu HPLC with a Supelcogel C-610H column of 30 cm × 7.8 mm ID was employed to separate both the carboxylic acids and alcohols in water. In addition, a UV (LC-20AB) and a RID-10A detectors were employed for quantitative chemical species analysis at various irradiation times. This was done with the intent of tracking the formation of organic acids and ethanol degradation during hydrogen production.

3. Results and discussions

3.1. BLB irradiation lamp characterization

The performance of artificially powered photocatalytic reactors is strongly influenced by the lamp irradiation spectra. Furthermore, it is advisable that the lamp to be used be warmed up for a period of 5 min to stabilize the lamp's emissions, before lamp utilization [24]. A StellarNet EPP2000C-25 LT16 Spectrometer was used to determine the energy spectrum of the BLB lamp through the fused silica windows in the Photo CREC Water II Reactor.

Fig. 2 displays a typical near-UV irradiation BLB characteristic spectrum emitted in the range of 340–410 nm. This is a BLB polychromatic lamp which emits photons having a wavelength which changes to a relatively narrow wavelength.

Once the irradiation is defined as in Fig. 2, the average emitted photon energy (E_{av}) can be calculated using the following relationship [30]:

$$E_{av} = \frac{\int_{\lambda_{min}}^{\lambda_{max}} I(\lambda)E(\lambda)\,d\lambda}{\int_{\lambda_{min}}^{\lambda_{max}} I(\lambda)\,d(\lambda)} \qquad (1)$$

In the case of this study and as shown in Fig. 2, all photons had a wavelength with a corresponding energy large enough to supersede the band gap of the Pt modified photocatalyst. Thus, all emitted photons were able in principle to contribute to the photocatalytic transformation. As a result, considering $E(\lambda) = hc/\lambda$ and the numerical integration of Eq. (1), the average photon energy is $E_{av} = 324.1$ kJ/photon.

In this respect, radiation distribution along the reactor axis in the Photo CREC Reactor was also measured using a lamp testing unit (LTU). Fig. 3 reports the irradiation axial fluxes for: (1) a
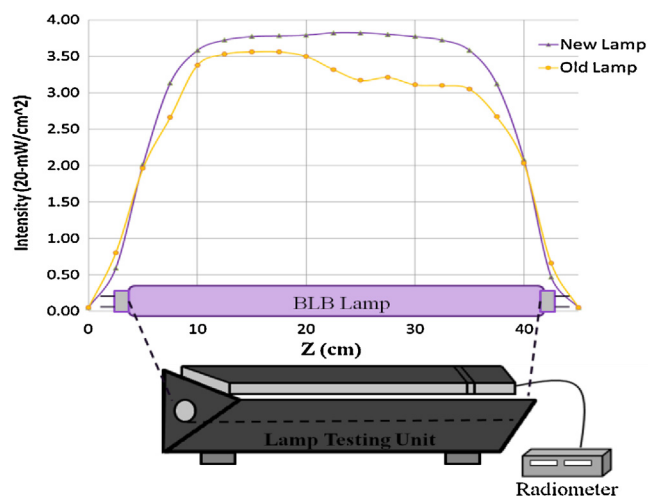
Fig. 3. Radiative axial flux distribution from an USHIO BLB lamp and a lamp testing unit.

new lamp: a symmetrical irradiation distribution case showing a stable irradiative flux along the reactor axis and (2) an old lamp (250 h of use): an asymmetric irradiation distribution, displaying axial changes of irradiation. This last case represents lamp performance decay observed after more than 100 h of operation. Lamps displaying "old lamp" irradiation distribution were excluded from the experimental runs of hydrogen production.

3.2. Photocatalyst characterization

3.2.1. BET surface area

The specific surface areas of all the prepared photocatalysts were determined employing a BET surface area analyzer (Micrometrics, ASAP 2010). This analyzer uses nitrogen adsorption–desorption isotherms.

Fig. 4 reports the BET specific surface areas for fresh DP25 (as received) and DP25 after thermal treatment at 450 °C: cases A and B, respectively. These cases show specific surface areas of 50.8 and 53.3 m^2/g. In addition, Fig. 4 reports the specific surface areas for Pt loaded TiO$_2$ with 0.06, 0.1, 0.2 and 1 wt% of platinum. Resulting specific surface areas (cases C, D, E and F) are 53.0, 53.2, 53.9 and 53.9 m^2/g, respectively. It is thus, possible to notice that Pt addition on DP25 slightly increases the specific surface area. Therefore, Pt loading of DP25 does not influence the specific surface significantly, and this parameter is not affected either by platinum loading or/and calcination.
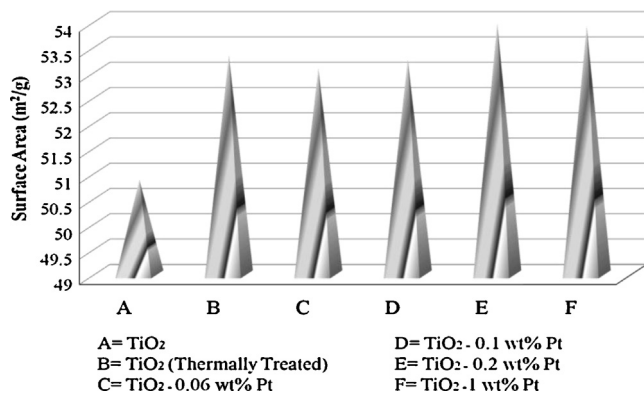

A= TiO$_2$
B= TiO$_2$ (Thermally Treated)
C= TiO$_2$ - 0.06 wt% Pt
D= TiO$_2$ - 0.1 wt% Pt
E= TiO$_2$ - 0.2 wt% Pt
F= TiO$_2$ - 1 wt% Pt

Fig. 4. Brunauer–Emmett–Teller (BET) specific surface areas for different TiO$_2$ samples.

Table 2
Pt crystallite size and Pt metal dispersion on DP25 at different metal loadings.

Photocatalyst	Weight % of Pt loaded	Active particle diameter (nm)	Metal dispersion (%)
DP25	0.06	2.68	42.21
	0.1	3.15	35.92
	0.2	3.42	33.15
	1	4.98	22.76

3.2.2. Chemisorption

Table 2 reports the results for different photocatalysts using pulse chemisorption. The photocatalysts of the present study were assessed using chemisorption measuring the percent of metal dispersion and the active platinum crystallite diameter at different Pt loadings on DP25. It was observed that at high platinum loadings, the metal dispersion on DP25 was reduced from 42.21 to 22.76%. This means that the platinum modified photocatalysts of this study provide good metal dispersion on DP25. Moreover, platinum crystallite sizes were increased with platinum loading from 2.68 to 4.98 nm. This is consistent with results reported later in this study: XRD suggests that platinum crystallites are smaller than 5 nm with no XRD characteristic 2θ peaks for Pt in the XRD diffractogram.

It is expected that higher platinum loadings on DP25 may improve charge distribution in the water-particle suspension, reducing TiO$_2$ particle agglomeration, as it is shown later in Section 3.2.5. However, higher platinum loadings if uncontrolled may favor e$^-$/h$^+$ recombination. Thus, one should expect an optimum value for platinum loadings on DP25 in terms of their influence for hydrogen production.

3.2.3. X-ray fluorescence (XRF)

Table 3 reports XRF analysis of Pt loadings. It can be noticed that the platinum on DP25 using incipient wetness impregnation was successful. The adopted impregnation method indeed provides the expected metal loadings on DP25. XRF determined loadings were 0.0616, 0.103, 0.23 and 1.08 wt%. These loadings were in close agreement with the ones anticipated.

3.2.4. X-ray diffraction (XRD)

The crystalline phases of the photocatalysts were investigated by an X-ray diffractometer RIGAKU Ultima IV a Multi-Purpose Diffractometer. (This instrument features a 3-kW X-ray beam with a high-precision θ–θ wide-angle horizontal goniometer and "cross beam optics".)

Fig. 5 reports the crystalline diffractogram patterns for DP25 (bare TiO$_2$) and for four other photocatalysts modified with Pt. XRD diffractograms were overlapped for comparison. One can note that the characteristic 2θ diffraction anatase peaks at 25°, 37°, 48°, 54° and 55° were consistently observed. The smaller XRD peaks at 27° and 69° were also present, given the rutile content in DP25. There were no other XRD peaks as one could expect for platinum at 40° and 46° of 2θ values [43,44].

These findings are consistent with the low platinum loadings on DP25 TiO$_2$. It is also confirmed that incipient wetness impregnation yields a highly dispersed metallic phase with smaller than

Table 3
XRF data of Pt loaded on DP25 particles.

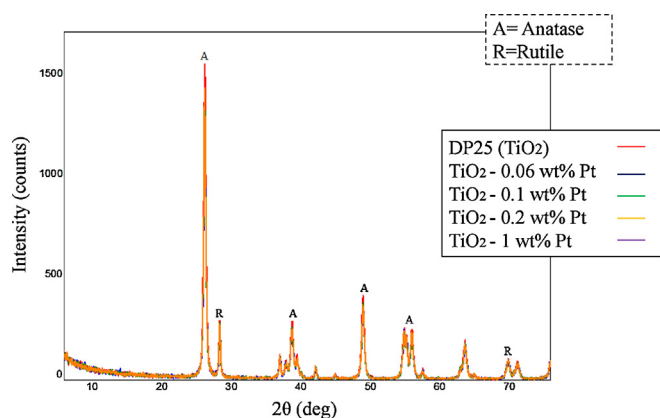| Photocatalyst	Weight % of Pt loaded	
	Expected	Determined
DP25	0.06	0.0616
	0.1	0.103
	0.2	0.23
	1	1.08

Fig. 5. XRD Diffractograms for DP25 (TiO$_2$) and Pt/TiO$_2$ photocatalysts, Furthermore, using Eq. (2), one can calculate the rutile content of DP25 (TiO$_2$) based on the XRD peak intensities [42].

Fig. 6. Particle size distribution chart by volume comparing DP25 (TiO$_2$) with different photocatalysts of Pt.

5 nm platinum crystallites, with these small crystallites passing undetected to XRD.

$$x = \left(1 + \frac{0.8I_A}{I_R}\right)^{-1} \qquad (2)$$

with x being the weight fraction of rutile in the TiO$_2$ powder, I_A and I_R being the XRD intensities for anatase and the rutile peaks, respectively.

Thus, with Eq. (2), it was possible to establish that DP25 contains 87% of anatase and 13% of rutile and that both phases were present in the commercial DP25 (TiO$_2$) and Pt modified TiO$_2$.

3.2.5. Particle size distribution (PSD)

Fig. 6 reports the particle size distribution (PSD) of DP25 (TiO$_2$) and the platinum-loaded TiO$_2$. It can be observed from the PSD chart, that Degussa P25 displays a significant fraction of particles in the 1000–3000 nm range even after sonication. However, when Degussa P25 was impregnated with Pt at 0.06, 0.1, 0.2 and 1 wt% loadings, there was a noticeable PSD displacement of the peaks toward the smaller particle sizes in the 50–100 nm range. Thus, it appears that Pt addition helps to reduce particle agglomeration, favoring better distribution of charges and as a result, interparticle surface forces [49,50]. While this effect may be in principle favorable in terms of irradiation absorption, it may also provide an enhanced electron (e$^-$)/hole (h$^+$) recombination reducing the effectiveness of hydrogen production.

3.2.6. Scan electron microscope and EDX

Images and elemental mapping of the photocatalyst were performed using SEM/EDX (LEO/Zeiss 154XB FIB/SEM). Fig. 7 shows SEM images of (a) DP25 (TiO$_2$) and (b) TiO$_2$ loaded with platinum.
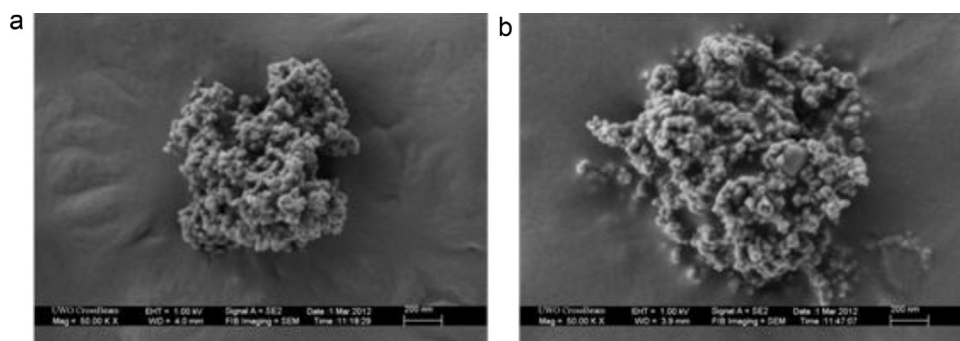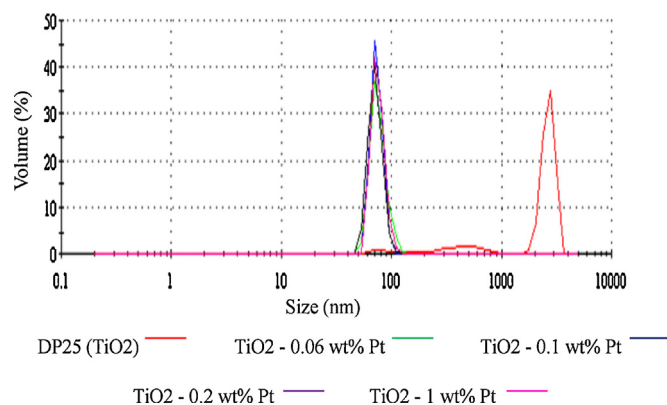
Individual Pt crystallites were difficult to be observe using SEM [28]. It can be seen, however, that there is particle agglomeration in DP25 strongly influenced by interparticle surface forces. Image (a) reports tighter agglomerates in bare DP25 while image (b) shows looser particle agglomerates for platinum doped DP25 particles. Thus, SEM confirms PSD observations where Pt addition reduces interparticle surface forces [49].

3.2.7. Diffuse reflectance UV–vis spectroscopy (DRS)

Platinum addition enhances irradiation absorption in the visible range. One can certainly see that there is a color change accompanying platinum addition treated by incipient wetness impregnation followed by calcination and reduction. The photocatalyst turns from light yellow to gray [11,32,34].

Fig. 8 represents schematically the effect of platinum loading on DP25 band gap energy. It can be hypothesized that platinum doping on DP25 introduces additional electron energy levels (Fermi level) into the conduction band [33,35,37,39]. This ends by yielding a reduction of the energy band gap level, as shown in the ensuing discussion from 3.20 to 2.73 eV.

Fig. 9 reports the diffuse reflectance UV–vis spectra for non-doped and platinum doped DP25. This UV–vis spectra provides both an indication of the UV–vis light semiconductor absorption, as well as a method for evaluating the band gap energy [36,40,41]. This method is based on extrapolating the spectrum steepest line of each UV–vis spectra until the wavelength axis is intersected (x-axis in Fig. 9). This intersection wavelength defines the band gap energy for the semiconductor under consideration as $E_{bg} = hc/\lambda_{int}$.

Using this method, one can notice that platinum addition progressively reduces UV–vis light absorption. In addition, the wavelength resulting from the extrapolation with the steepest line gives a λ_{int} of 388 nm or 3.2 eV for DP25 and 455 nm or 2.73 eV for platinum modified DP25 with 1 wt% of Pt.

Fig. 7. SEM images of (a) DP25 (TiO$_2$) and (b) TiO$_2$ loaded with Pt.
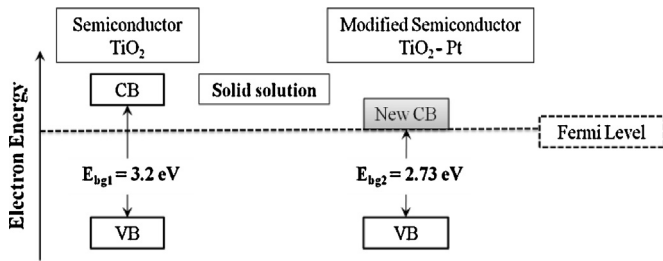
Fig. 8. Schematic representation of energy band gaps and energy band gap reduction as a result of the Pt doping on TiO_2.

Thus, one can conclude that photon absorption is related to the amount of Pt^0 present on the photocatalyst surface [36]. Furthermore, platinum addition provides semiconductors with a wider irradiation absorption spectrum, absorbing photons with lower energy [47,49]. It is expected on this basis, that platinum addition on DP25 will provide an enhanced photocatalytic activity for hydrogen production [11,27,31,38,49].

3.2.8. Local volumetric rate of energy absorption (LVREA)

LVREA can be determined experimentally through the irradiation intensity macroscopic balance inside the photocatalytic reactor. In this respect, chemical actinometry provides insufficient assessment of LVREA given that it assumes that photons not reaching the outer reactor wall are absorbed. Instead, a macroscopic radiation balance allows the calculation of the precise radiation absorbed by the solid photocatalyst [29,44,45].

Using this approach one can establish the optimal photocatalyst concentration allowing all forward radiation contained in the slurry photocatalyst phase in the Photo CREC units [45].

3.2.8.1. Macroscopic radiation energy balance (MREB).
A macroscopic energy balance can be applied to a control volume as described in Fig. 10a). This control volume is established to include the semiconductor slurry phase [29,44]. It allows the evaluation of the rate of photon absorption as follows:

$$P_a = P_i - P_{bs} - P_t \tag{3}$$

where P_a is the rate of absorbed photons by the photocatalyst, P_i is the rate of photons reaching the reactor inner surface, P_{bs} is the
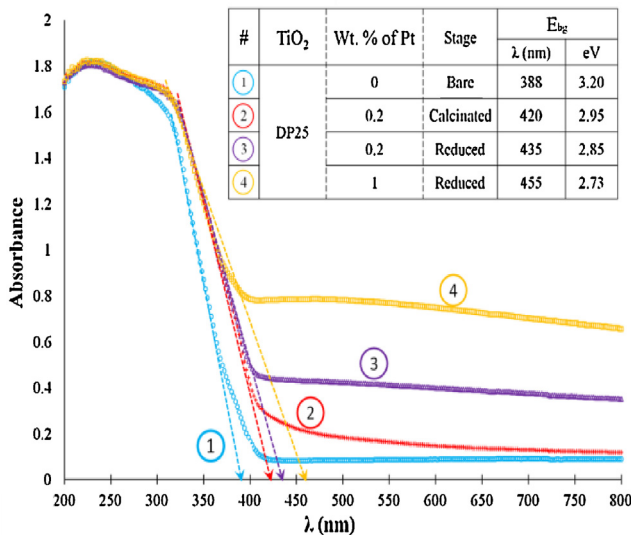

Fig. 9. Optical absorption spectra of DP25 (TiO_2) and platinum loaded TiO_2 at different conditions. This intersection wavelength defines the band gap energy for the semiconductor under consideration.
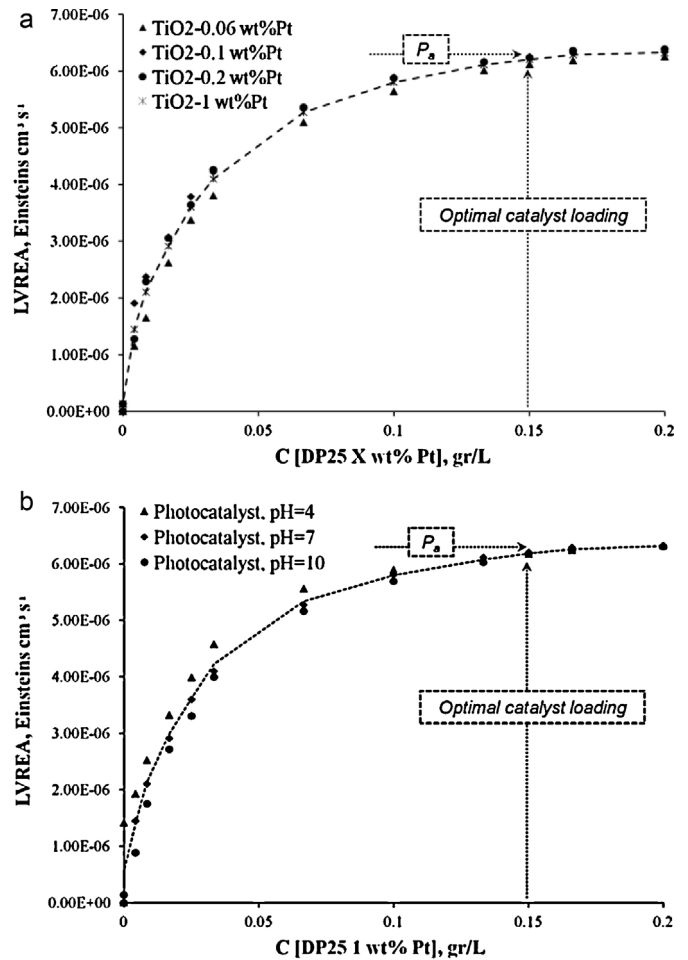

Fig. 10. (a) LVREA in the Photo CREC Water-II Reactor annular channel for various Pt loadings TiO_2 at pH = 7. Standard deviations for repeats at 4 axial positions: 2–4%. (b) LVREA inside the Photo CREC Water-II Reactor annular channel with 1 wt% Pt loading on TiO_2 at different pHs. Standard deviations for repeats at 4 axial positions: 2–3%.

rate of backscattered photons exiting the system, and P_t is the rate of transmitted photons (all in einsteins/s).

The various terms in Eq. (3) are calculated as follows:

(a) P_i can be evaluated from the difference between the rate of photons emitted by the lamp (P_o), and the rate of photons absorbed or back reflected by the inner Pyrex glass wall ($P_{a\text{-wall}}$)

$$P_i = P_o - P_{a\text{-wall}} \tag{4}$$

(b) P_o or the rate of photons emitted by the lamp can be calculated given the lamp BLB emission spectrum and radiometric measurements (refer to Fig. 2).

$$P_o = \int_{\lambda_1}^{\lambda_2} \int_0^L \int_0^{2\pi} q(\theta, z, \lambda) r \, d\theta \, dz \, d\lambda \tag{5}$$

(c) $P_{a\text{-wall}}$ can be computed from transmission measurements through the inner Pyrex tube. Fig. 2 also displays the very modest change of irradiation spectrum radiation that evolves through the inner Pyrex glass. The little energy band gap (λ_{Ebg}) changes introduced by the Pyrex glass are reported as well (Table 4).

Table 4
Pyrex glass transparency and BLB lamp emission rates.

Variable	Watts	Einsteins/s
P_o	3.98	1.242×10^{-5}
P_i	3.66	1.142×10^{-5}
P_{a-wall}	0.32	9.973×10^{-7}

(d) P_{bs} can be approximated by the difference between P_i and the rate of photons transmitted when the photocatalyst concentration approaches zero.

$$P_{bs} = P_i - P|_{c \to 0^+} \tag{6}$$

(e) P_t can be calculated as the addition of the transmitted non-scattered radiation (P_{ns}) and the forward scattering radiation (P_{fs}).

$$P_t = P_{ns} - P_{fsc} \tag{7}$$

Regarding P_{ns}, it can be estimated by using the black collimators for the transmitted non-scattered radiation, and P_{fs} can also be evaluated using polished-aluminum tube collimators. These two radiation terms account for the combined transmitted non-scattered radiation and forward-scattering radiation [29,45].

As a result and using this approach, one can establish in Fig. 10a and b that LVREA increases with photocatalyst concentration with a LVREA optimum achieved at 0.15 g for DP25 or modified DP25 per liter. At these conditions, one can secure 95% of the irradiated absorption. One can notice that this optimum value, as reported in Fig. 10a and b, is independent of both the pH and Pt loading.

Fig. 12. Schematic reaction mechanism for hydrogen production in a Photo CREC Water II Reactor using C_2H_5OH as sacrificial agent.

3.3. Hydrogen production

3.3.1. Photocatalytic reaction mechanism

Fig. 11 reports a schematic description of hydrogen production in the modified photo CREC unit. Fig. 11 provides representations at three different scales: macro-scale, meso-scale (Zoom 1) and micro-scale (Zoom 2). This schematic representation emphasizes the event that could occur at the level of a doped TiO_2 particle (meso-scale) and on a surface region where platinum crystallite is laid out (micro-scale). Irradiation of this zone, as described in Zoom 2, leads to charge separation (e^- and h^+ sites). This elementary step is the preamble to $H^\bullet$ formation.

Thus, in the Photo CREC Water II Reactor, with suspended and impregnated-TiO_2 particles and a water solution containing an organic scavenger such as ethanol, the following mechanistic steps can be considered (refer to Fig. 12 and manuscript Appendix A): (i) a photon reaches the semiconductor surface with an energy greater than the band gap, (ii) an electron (e^-) and a hole (h^+)
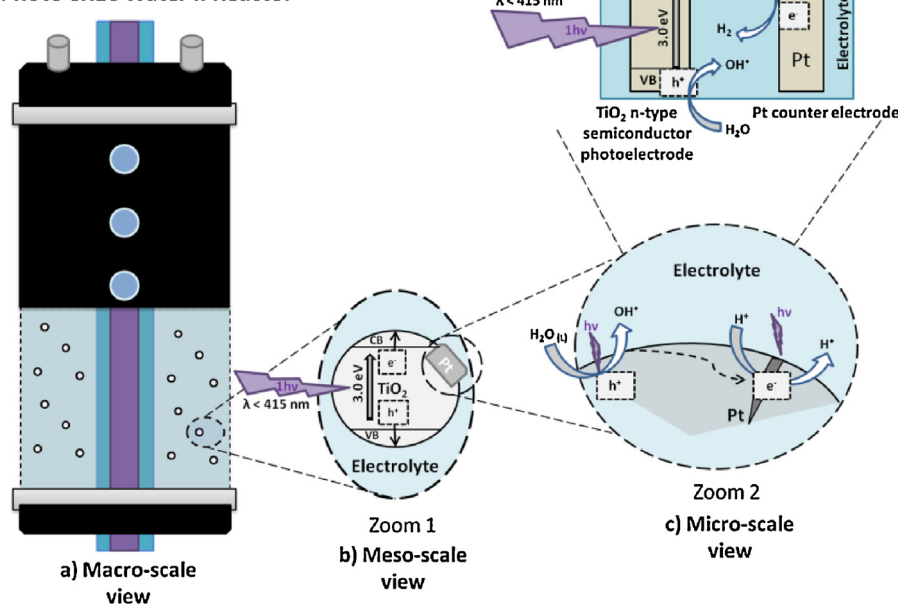

Fig. 11. Description of the photocatalytic reaction steps taking place in a Photo CREC Water II Unit for hydrogen production showing views of the (a) macro-scale, (b) meso-scale, and (c) micro-scale.
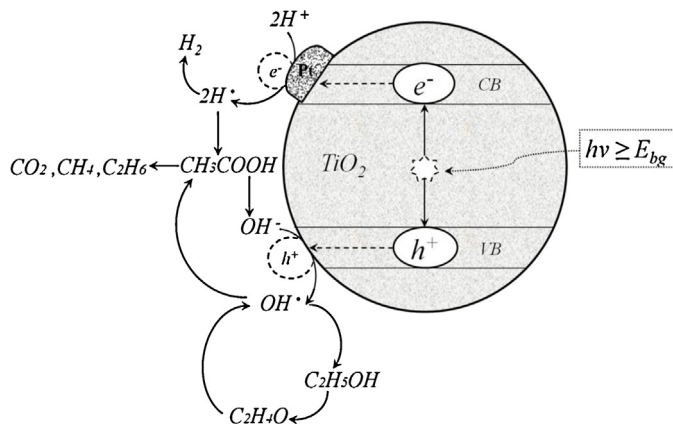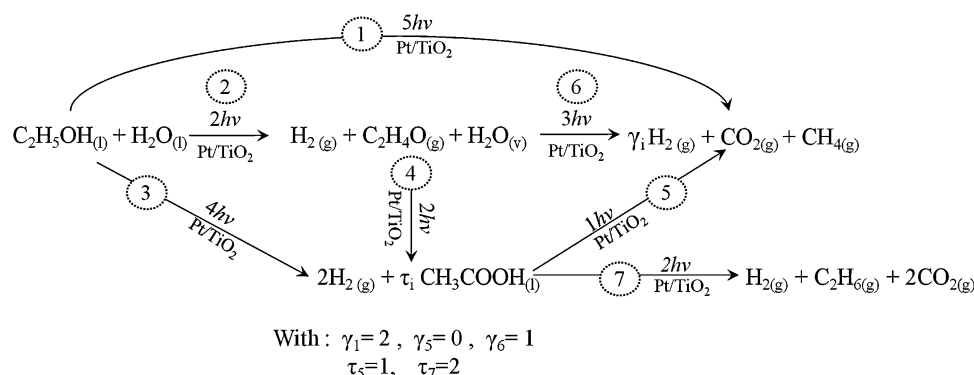
Fig. 13. Reaction network for hydrogen production when using ethanol as an organic scavenger. γ_i and τ_i refer to the stoichiometric coefficients for steps "i" in the reaction network.

separate, given the electron energy content to allow charges to move from the valence band to the conduction band, (iii) platinum nanoparticles deposited on the surface of DP25 (TiO_2) act as electron reservoirs, capturing the moving electrons on the DP25 (TiO_2) surface [6,7,13,19,21], (iv) stored electrons interact with adsorbed protons, formed from dissociated water yielding H• radicals, (v) hydrogen radicals couple themselves forming gas phase hydrogen ($H_{2(g)}$).

On the other hand, the produced h^+ holes react with OH^- groups forming OH• radicals. These hydroxyl radicals (OH•) are highly reactive species, able to convert ethanol (C_2H_5OH) or other organic species (refer to Fig. 12 and Appendix A). Regarding the ethanol reaction with OH• species, ethanol can form acetaldehyde (C_2H_4O) in the first reaction step of the network. This reaction step can be followed by further reaction of acetaldehyde with another OH• yielding acetic acid (CH_3COOH). Moreover, formed acetic acid can be further converted under the prevalent conditions of the Photo CREC Water II into carbon monoxide (CO_2), methane (CH_4) and ethane (C_2H_6).

In competition with the above described reaction steps, there is a possible e^- and h^+ site recombination. This electron and hole recombination does not accomplish any useful photocatalytic conversion, and as a consequence contributes to the overall photocatalytic process inefficiency. Thus, e^-/h^+ recombination has to be limited as much as possible.

3.3.2. The energy efficiency factors in photocatalytic processes

Energy efficiency criteria in a photochemical process such as Quantum Yields (QY) are critical parameters in establishing irradiation utilization [24].

3.3.2.1. Quantum yield for hydrogen production (φ).
The quantum yield (QY) for hydrogen production is a number ratio resulting from equating the rate of H• molecules produced over the number of photons absorbed in the impregnated TiO_2 [24,46]:

$$\%\varphi = \frac{[dN_i/dt]}{P_a} \times 100 \tag{8}$$

Fig. 13 describes a "*series–parallel*" model already postulated for the photoconversion of organic pollutants in water in a Photo CREC Water II Reactor [24]. This reaction network is adapted in the present study for hydrogen production having ethanol as the "organic scavenger". This mechanism is expected given the likely variability of photon density as in a Photo CREC Water II Reactor.

One can see that as reported in Table 5 and as described in detail in Appendices A and B, one can define the "*theoretical quantum yields*" based on the photon stoichiometric requirements for H• radical production as follows:

$$\varphi_{\text{theor}} = \frac{\text{moles of H}^\bullet}{\text{moles of photons}} \tag{9}$$

For instance, in the case of complete mineralization of ethanol, this "*theoretical quantum yield*" is 0.8. However, considering the possible influence of various reaction steps at any time during the irradiation process with these steps involving both the scavenger and the intermediates, a reasonable average estimate for this theoretical QY is 0.78 or 78%. It should be emphasized that this theoretical QY value can be used as a reference only, and represents the QY that one can expect assuming that there is no electron–hole recombination.

3.3.3. Effect of the pH on hydrogen production and on Quantum Yields (φ)

Both hydrogen and photo energy efficiencies (% φ) were determined at NTP normal conditions (ambient temperature and close to atmospheric pressure) for different pHs [3] and different Pt loadings [28,31,32,34,47]. Each experiment was developed as follows: (i) near UV lamp off: 30 min period with argon circulated continuously to remove any remaining oxygen from air and until ethanol adsorption equilibrium on doped TiO_2 was reached; (2) near UV lamp on: 5 h period where water with a suspended photocatalyst was recalculated continuously under irradiation. During both lamp off and lamp on, irradiation periods samples were taken periodically and analyzed in an HPLC and GC. This process allows one to establish the influence of Pt loading on the doped TiO_2 and the effect of operating parameters (e.g. pH) on quantum yields.

Table 5
Description of theoretical quantum yields for the various steps involved in the conversion of ethanol as the organic scavenger for hydrogen production.

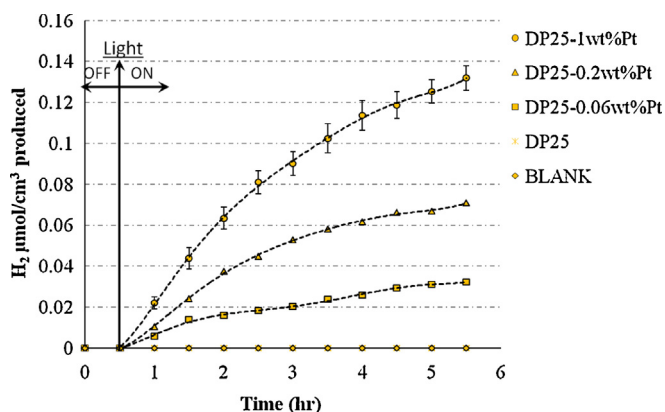| Reaction path	Reactant	Product	Photons ($h\nu$)	H_2 formed	φ_{theor} = H•/photons	Refer to the following equation in Appendix
1	C_2H_5OH	CH_4, CO_2	5	2	0.8	(A.27)
2	C_2H_5OH	C_2H_4O	2	1	1	(A.11)
3	C_2H_5OH	C_2H_3OOH	4	2	1	(A.17)
4	C_2H_4O	C_2H_3OOH	2	1	1	(A.15)
5	CH_3COOH	CH_4, CO_2	1	0	0	(A.21)
6	C_2H_4O	CH_4, CO_2	3	1	0.666	(A.29)
7	$2CH_3COOH$	C_2H_6, CO_2	2	2	1	(A.25)

Fig. 14. Hydrogen profiles at different Pt loadings on DP25, pH = 10, ethanol (2 v/v%) as purging gas; trend line (–). Bars in this graph represent standard deviations on repeats.

3.3.3.1. Effect of alkaline pH. A 2 M NaOH solution was prepared and 2 ml of this solution were added to 6 L water/2 vol.% ethanol solution. This solution was placed in the Photo CREC Water II mixing tank. The resulting pH before the experiment was approximately 10, and remained essentially unchanged during the complete experimental run.

Fig. 14 displays the cumulative hydrogen generation at various irradiation times and at various platinum loadings for a pH of 10. It can be observed that at the alkaline conditions of pH = 10, the 1 wt% loading provides the best hydrogen generation performance of the four photocatalysts considered.

All these photocatalysts, as described in Fig. 14, display a number of common features in terms of hydrogen production as follows: (i) the rates of hydrogen production were consistently higher during the first 1.5 h of the run and (ii) the rates of hydrogen production decreased consistently after the initial 1.5 h run period. Thus, it appears that the platinum–TiO_2 under alkaline pHs still allows hydrogen production under the high OH^- and limited H^+ concentrations, as one can expect from water equilibrium dissociation. However, it is also possible to observe that while the run is progressing, this limited availability of H^+ becomes even more acute on the photocatalyst surface with this leading to a progressive reduction of hydrogen formation rates.

Fig. 15 reports the Quantum Yields for a pH = 10. QYs were determined using Eqs. (3) and (8), and the respective values of hydrogen formation rates. It is important to notice that the reported QYs are based on $H^\bullet$ generation rates, whereby it is observed that the two phases for QYs are as follows: (a) QYs increase reaching a maximum
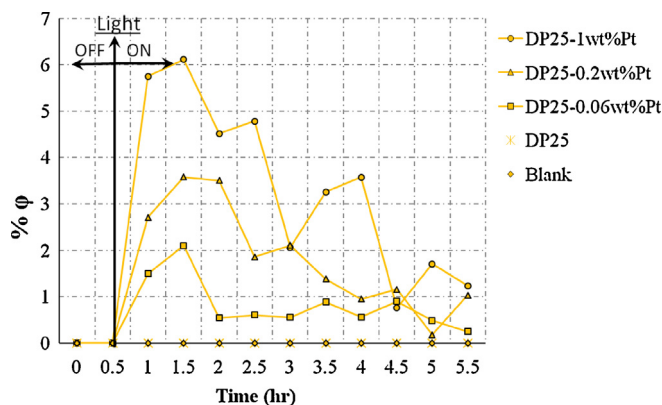
value in between 1 and 2 h of irradiation and (b) QYs steadily decline during the remaining period of the run.

Table 6 reports hydrogen reaction rates and Quantum Yields (φ) for three of the photocatalysts of this study using a Photo CREC Water II Reactor. One can see that all of the Pt impregnated Degussa P25 photocatalysts display a higher hydrogen production than the bare Degussa P25. Thus, it is shown that platinum addition on DP25 having ethanol as the organic scavenger allows hydrogen production with a maximum 280 mol/h · g_{cat} rate during the 1–2 h irradiation period and a 5.7% quantum yield.

3.3.3.2. Effect of neutral pH. Experiments were developed with the various photocatalysts with a pH of 7. The pH remained close to the original value during the entire 5.5 h of the run.

Fig. 16 shows the cumulative hydrogen formation. Hydrogen production was detected as soon as the near UV lamp was turned on with cumulative hydrogen formed increasingly during the whole run. It can be observed that at a pH = 7, there is a consistent increase of hydrogen during the first 1.5 h, with this increase being more modest for the remaining run period. This trend appears to be similar to the one observed at pH = 10.

Fig. 17 reports QYs for the various photocatalysts at pHs of 7. One can notice that similar QY trends as the ones observed at pH = 10 are obtained. In fact, in all the studies, photocatalysts display a common trend: (a) a QY increase during the first 1.5 h, and then (b) a QY reduction for the rest of the run.

Table 7 reports hydrogen reaction rates and Quantum Yields (φ) in a Photo CREC Water II Reactor for four different photocatalysts at pH = 7. It is proven that platinum impregnated DP25 in the presence of the ethanol scavenger allows hydrogen production. Furthermore, it is also noticed that the 1 wt% Pt addition yields a maximum hydrogen formation rate of 226 mol/h · g_{cat} with a 4.6 QY. This QY is close to the best 5.7% of the QY achieved at alkaline conditions.

3.3.3.3. Effect of acid pH. The influence of acid pH on hydrogen formation rate was studied using H_2SO_4 [2 M]. 1 ml of this sulfuric

Table 6
Reaction rates at different loadings of Pt on TiO_2 and pH = 10 in the Photo-CREC Reactor.

Catalyst	Reaction rate[a] (mol h^{-1} g_{cat}^{-1})	Quantum yield (% φ) H_2 production
DP25 0.06 wt% Pt	73	1.5
DP25 0.2 wt% Pt	132	2.7
DP25 1 wt% Pt	280	5.7

[a] Reaction conditions: 298 K, 1 atm.

Fig. 15. Overall QY calculations at different Pt loadings on DP25, pH = 10, EtOH (2 v/v%) and argon as purging gas.
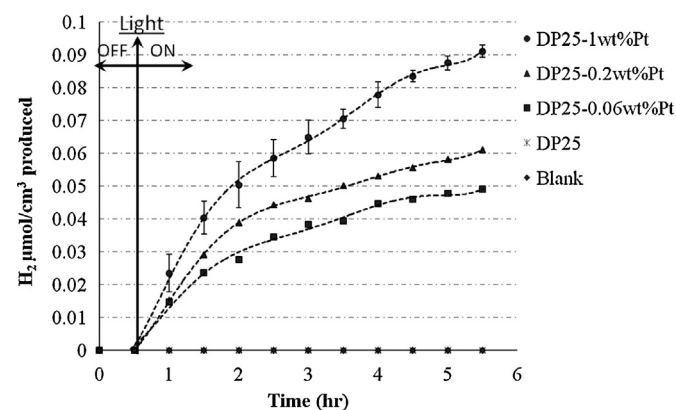

Fig. 16. Hydrogen profiles at different Pt loadings on DP25, pH = 7, EtOH (2 v/v%) and argon as purging gas; trend line (–). Bars in this graph represent standard deviations on repeats.
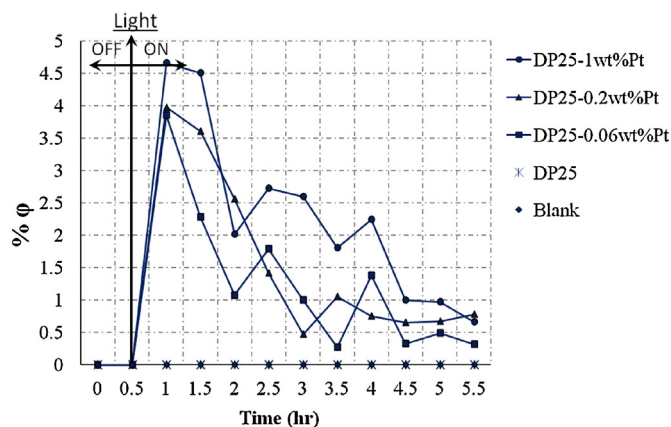
Fig. 17. Overall QY calculations at different Pt loadings on DP25, pH = 7, EtOH (2 v/v%) and using argon as purging gas.

Table 7
Reaction rates at different loadings of Pt on TiO_2 and a pH = 7 in the Photo-CREC II Reactor.

Catalyst	Reaction rate[a] (mol h^{-1} g$_{cat}^{-1}$)	Quantum yield (% φ) H_2 production
DP25 0.06 wt% Pt	188	3.8
DP25 0.2 wt% Pt	193	3.9
DP25 1 wt% Pt	226	4.6

[a] Reaction conditions: 298 K, 1 atm.

acid solution was added in the 6 L tank containing a water/ethanol solution. Regarding the pH, it was observed that it remained close to 4 for the complete 5.5 h of the experiment duration.

Fig. 18 displays the cumulative hydrogen production for different Pt loadings on DP25. As soon as the lamp was turned on, hydrogen formation was observed. A common and distinctive trend for the cumulative hydrogen formation curves is that they were consistently linear. In this respect, the linear trend was a major difference vis-a-vis of results obtained with the samples having a pH of 7 and 10. In particular, one can also notice in Fig. 18 that 1 wt% Pt loading led to the best hydrogen production under acidic conditions.

Fig. 19 reports the QY for the pH of 4. It was observed that there were distinctive trends of QYs once the near UV lamp was on: (i) progressive increase of hydrogen formation rate and as a consequence of the QYs during the first half an hour of irradiation and (ii) steady hydrogen formation rate during 5.5 h with a ethanol
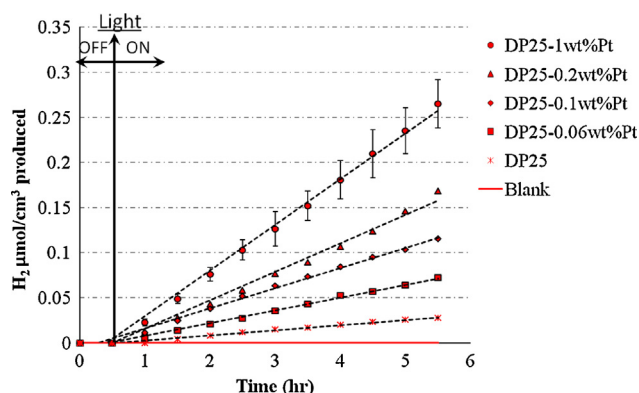

Fig. 18. Hydrogen profiles at different Pt loadings on DP25, pH = 4, EtOH (2 v/v%) and argon as purging gas; trend line (–). Bars in this graph represent standard deviations on repeats.
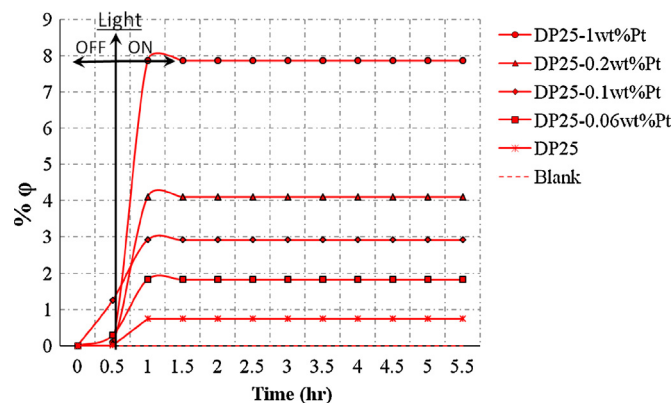

Fig. 19. Overall QY calculations at different Pt loadings on DP25, pH = 4, EtOH (2 v/v%) and using argon as purging gas.

conversion of less than 15%. As a result QYs reach maximum values after 0.5 h and remain at those levels for the rest of the run.

As described in Figs. 18 and 19, four different samples of DP25 loaded with platinum were considered in the experimental runs at a pH of 4. The photocatalysts studied, all showed steady hydrogen formation rates after the first half an hour of irradiation, will all of them surpassing the QYs of the bare Degussa D25.

Table 8 reports hydrogen formation rates and Quantum Yields (φ) in the Photo CREC Water II Reactor for the four different Pt modified photocatalysts at pH = 4. It can be observed that a 383 mol/h·g$_{cat}$ hydrogen formation rate is obtained in between 1 and 2 h of irradiation with a corresponding 7.86% quantum yield. This value remains steady during the 5.5 h of the run.

As a consequence, we can see that at a pH = 4, the gas phase achieved a significantly increased hydrogen content during the 5.5 h experiment. Therefore, it appears that the high concentration of H$^+$ ions in the acid aqueous solution favors water dissociation and formation of hydronium ions. Additionally, the protons adsorbed on the photocatalyst can easily interact with generated and stored electrons, promoting hydrogen formation [48].

It is interesting to notice that the rate of hydrogen formation under acid pH becomes a steady process: H$^+$ ions from the solution can be quickly resupplied to the photocatalyst surface (see Appendix B). As a result, there is no decay in hydrogen formation rates under acidic conditions and the cumulative hydrogen formation continues to increase without noticeable decline. This is, in our view, a valuable finding which is in clear contrast with the results obtained in the case of alkaline and neutral pH solutions where H$^+$ ion resupply appears to be limited.

In addition, one should note that the 7.8% QYs using Pt impregnated DP25 in a Photo CREC Water II under acidic conditions, are still valuable. This is the case in spite of being smaller than the expected theoretical 78% QY for hydrogen production (refer to Section 3.3.2.1). This QY which is lower than the theoretical value can be justified given H$^\bullet$ formation via photocatalysis using organic scavengers likely requires a 2 photon consecutive process [54].

Table 8
Reaction rates at different loadings of Pt on TiO_2 and pH = 4 in the Photo CREC Water II Reactor.

Catalyst	Reaction rate[a] (mol h^{-1} g$_{cat}^{-1}$)	Quantum yield (% φ) H_2 production
DP25	36	0.7
DP25 0.06 wt% Pt	89	1.8
DP25 0.1 wt% Pt	142	2.9
DP25 0.2 wt% Pt	200	4.1
DP25 1 wt% Pt	383	7.9

[a] Reaction conditions: 298 K, 1 atm.

4. Conclusions

(a) It is shown that an upgraded Photo CREC Water II Reactor can be used advantageously for storing and producing hydrogen for water splitting. The irradiative axial flux distribution and the irradiation spectrum for the BLB UV lamp were considered in this reactor using a lamp calibration unit and a spectrometer radiometer.

(b) It is proven that TiO_2 loaded with Pt using incipient wetness reduces particle agglomeration and presumably favors a better distribution of e^-/h^+, limiting charge recombinations, which is a favorable condition for water splitting. Furthermore, platinum addition reduces the band gap of DP25 (TiO_2) from 3.20 eV to 2.73 eV.

(c) It is shown that by means of macroscopic radiation energy balances in the Photo CREC Water II Unit, the LVREA for the various photocatalysts of this study can be established. As a result, a best photocatalyst loading of 0.15 g/L was considered.

(d) It is demonstrated that DP25 loaded with Pt in the presence of a sacrificial agent such as ethanol, favors free oxygen formation of hydrogen via photocatalysis.

(e) It is shown that hydrogen forms at different pHs. It is proven, however, that acidic conditions are the most suitable for yielding both steady hydrogen formation rates and best quantum yields.

Acknowledgments

Appendix A. Theoretical quantum efficiency for hydrogen production

A.1. Common steps during photocatalytic processes

A reaction mechanism can be established based on the photocatalytic reaction steps as adapted for hydrogen production.

Step a.1 *Dark Period*: During the period that lights are off, adsorption of both organic molecules and water take place on the TiO_2 surface as follows:

$$\text{Organic Molecule}_{(l)} \xrightarrow{TiO_2-Pt} \text{Organic Molecule}_{(ads)} \tag{A.1}$$

$$H_2O_{(l)} \xrightarrow{TiO_2-Pt} H_2O_{(ads)} \tag{A.2}$$

Step a.2 *Irradiation Period-Separation of Charges*: The light is "on" for an extended period with photoreactions taking place as a result. Photons with the right energy intensity excites the TiO_2 particles as follows,

$$h\nu \xrightarrow{TiO_2-Pt} h^+ + e^- \tag{A.3}$$

Step a.3 *Irradiation Period-Formation of OH• radicals*. There is dissociation of water adsorbed molecules. Furthermore, electron holes react with adsorbed OH^- hydroxyl ions adsorbed on the surface of TiO_2 producing hydroxyl radicals as follows:

$$H_2O_{(ads)} \xrightarrow{TiO_2-Pt} H^+_{(ads)} + OH^-_{(ads)} \tag{A.4}$$

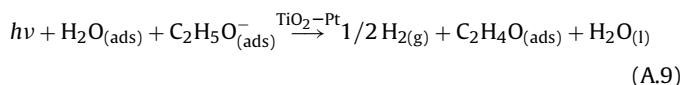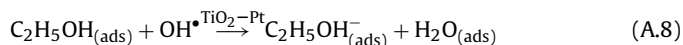$$OH^-_{(ads)} + h^+ \xrightarrow{TiO_2-Pt} OH^• \tag{A.5}$$

Step a.4 *Irradiation Period-Formation of H• radicals*. Platinum acts as an electron reservoir loaded on TiO_2 surfaces. In this respect, protons present on the TiO_2 surface form H• radicals with this leading to hydrogen (H_2) formation as follows:

$$H^+_{(ads)} + e^- \xrightarrow{TiO_2-Pt} H^• \tag{A.6}$$

$$H^• \xrightarrow{TiO_2-Pt} 1/2\, H_{2(g)} \tag{A.7}$$
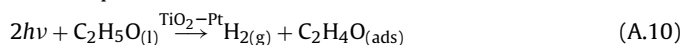
A.2. Ethanol conversion into acetaldehyde

Step b.1 *Irradiation Period-Hydroxyl radicals are consumed by the organic scavenger (ethanol) producing acetaldehyde*,

$$C_2H_5OH_{(ads)} + OH^• \xrightarrow{TiO_2-Pt} C_2H_5OH^-_{(ads)} + H_2O_{(ads)} \tag{A.8}$$

$$h\nu + H_2O_{(ads)} + C_2H_5O^-_{(ads)} \xrightarrow{TiO_2-Pt} 1/2\, H_{2(g)} + C_2H_4O_{(ads)} + H_2O_{(l)} \tag{A.9}$$

Addition of Eqs. (A.2)–(A.9) yields the following overall stoichiometric equation,

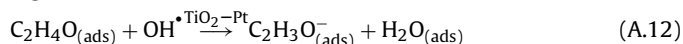$$2h\nu + C_2H_5O_{(l)} \xrightarrow{TiO_2-Pt} H_{2(g)} + C_2H_4O_{(ads)} \tag{A.10}$$

Thus, one can conclude that 2 photons are required to produce one H_2 molecule or two H• radicals. As a result, the maximum theoretical quantum efficiency based on the H• formed is 1 as follows:

$$\varphi_{\text{theor}} = \frac{\text{moles of H}^•}{\text{moles of photons}} = 1 \tag{A.11}$$
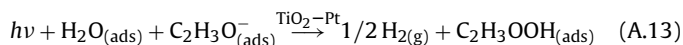
A.3. Acetaldehyde conversion into acetic acid

Step c.1 Irradiation Period-Hydroxyl radicals are consumed by the acetaldehyde producing acetic acid.

OH• radicals attack the adsorbed acetaldehyde molecules resulting in the formation of adsorbed enolate anions as follows,

$$C_2H_4O_{(ads)} + OH^• \xrightarrow{TiO_2-Pt} C_2H_3O^-_{(ads)} + H_2O_{(ads)} \tag{A.12}$$

The formed enolate reacts further with water yielding acetic acid,

$$h\nu + H_2O_{(ads)} + C_2H_3O^-_{(ads)} \xrightarrow{TiO_2-Pt} 1/2\, H_{2(g)} + C_2H_3OOH_{(ads)} \tag{A.13}$$

The addition of Eqs. (A.2)–(A.7), (A.12) and (A.13) gives the following overall stoichiometric equation,
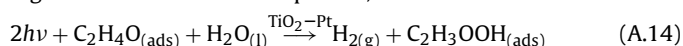
$$2h\nu + C_2H_4O_{(ads)} + H_2O_{(l)} \xrightarrow{TiO_2-Pt} H_{2(g)} + C_2H_3OOH_{(ads)} \tag{A.14}$$

Thus, one can conclude that 2 photons are required to produce one H_2 molecule or 2H• radicals. As a result, the maximum theoretical quantum efficiency based on the H• formed is 1 as follows:

$$\varphi_{\text{theor}} = \frac{\text{moles of H}^•}{\text{moles of photons}} = 1 \tag{A.15}$$

A.4. Ethanol conversion into acetic acid

Step d.1 Irradiation Period-Hydroxyl radicals are consumed by the organic scavenger (ethanol) producing acetic acid

The overall reaction assuming total mineralization of acetaldehyde can be reported as a summation of the reactions A.10 and A.14. This leads us to the overall stoichiometric expression as follows:

$$4h\nu + C_2H_5OH_{(l)} + H_2O_{(l)} \xrightarrow{TiO_2-Pt} 2H_{2(g)} + C_2H_3OOH \quad (A.16)$$
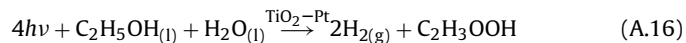
Thus, one can conclude that for the formation of two H_2 molecules requires four photons. As a result, the theoretical quantum efficiency for this step based on the $H^\bullet$ formed is 1 as follows:

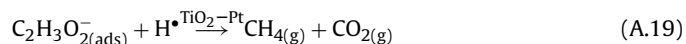$$\varphi_{theor} = \frac{\text{moles of } H^\bullet}{\text{moles of photons}} = 1 \quad (A.17)$$

A.5. Acetic acid conversion into methane and carbon dioxide

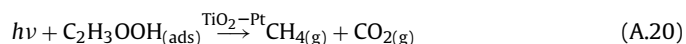Step e.1) Formed hydroxyl radicals react with adsorbed unimolecular acetic acid forming CO_2

Formed $OH^\bullet$ radicals react with the adsorbed acetic acid to form the acetate anion as follows [53],

$$C_2H_3OOH_{(ads)} + OH^\bullet \xrightarrow{TiO_2-Pt} C_2H_3O_{2(ads)}^- \quad (A.18)$$
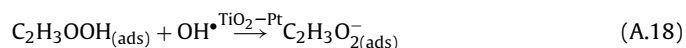
The formed $H^\bullet$ radical reacts with the acetate anion yielding methane and CO_2,

$$C_2H_3O_{2(ads)}^- + H^\bullet \xrightarrow{TiO_2-Pt} CH_{4(g)} + CO_{2(g)} \quad (A.19)$$

Addition of Eqs. (A.2)–(A.6), (A.16) and (A.19), leads to the following stoichiometric equation,

$$h\nu + C_2H_3OOH_{(ads)} \xrightarrow{TiO_2-Pt} CH_{4(g)} + CO_{2(g)} \quad (A.20)$$
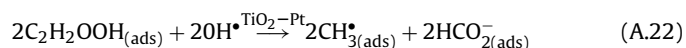
Thus, one can conclude that the photons required do not lead to H_2 formation. As a result, the theoretical quantum efficiency for this step based on the $H^\bullet$ formed is 0 as follows:

$$\varphi_{theor} = \frac{\text{moles of } H^\bullet}{\text{moles of photons}} = 0 \quad (A.21)$$

A.6. Acetic acid conversion into ethane and carbon dioxide

Step f.1 Formed hydroxyl radicals react with adsorbed bimolecular acetic acid forming H_2, C_2H_6 and CO_2.

Formed $OH^\bullet$ radicals react with the adsorbed bimolecular acetic acid to form the formate anion and the methyl radicals as follows [53],

$$2C_2H_2OOH_{(ads)} + 20H^\bullet \xrightarrow{TiO_2-Pt} 2CH_{3(ads)}^\bullet + 2HCO_{2(ads)}^- \quad (A.22)$$

The formed methyl radicals react between them yielding ethane and the formate anion it is broken down into carbon dioxide and hydrogen,

$$2CH_{3(ads)}^\bullet + 2HCO_{2(ads)}^- \xrightarrow{TiO_2-Pt} H_{2(g)} + C_2H_{6(g)} + 2CO_{2(g)} \quad (A.23)$$
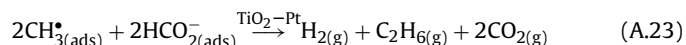
Addition of Eqs. (A.2)–(A.7), (A.22) and (A.23), leads to the following stoichiometric equation,
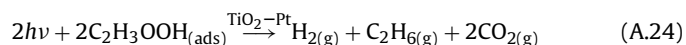
$$2h\nu + 2C_2H_3OOH_{(ads)} \xrightarrow{TiO_2-Pt} H_{2(g)} + C_2H_{6(g)} + 2CO_{2(g)} \quad (A.24)$$
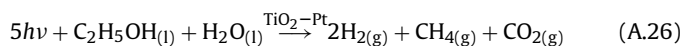
Thus, one can conclude that 2 photons are required to produce one H_2 molecule or $2H^\bullet$ radicals. As a result, the theoretical quantum efficiency for this step based on the $H^\bullet$ formed is 1 as follows:

$$\varphi_{theor} = \frac{\text{moles of } H^\bullet}{\text{moles of photons}} = 1 \quad (A.25)$$

A.7. Total mineralization of ethanol, acetaldehyde and acetic acid

Step g.1 Formed hydroxyl radicals react with adsorbed acetic acid forming CO_2

The overall reaction assuming total mineralization of ethanol can be reported as a summation of reactions (A.10), (A.14) and (A.20) leading us to the overall stoichiometric expression,

$$5h\nu + C_2H_5OH_{(l)} + H_2O_{(l)} \xrightarrow{TiO_2-Pt} 2H_{2(g)} + CH_{4(g)} + CO_{2(g)} \quad (A.26)$$

Thus, one can conclude that for the formation of two H_2 requires 5 photons. As a result, the theoretical quantum efficiency for this step, based in the $H^\bullet$ formed, is 0.8 as follows:

$$\varphi_{theor} = \frac{\text{moles of } H^\bullet}{\text{moles of Photons}} = 0.8 \quad (A.27)$$

Step g.2) Formed hydroxyl radicals react with adsorbed acetaldehyde forming CO_2

The overall reaction assuming total mineralization of acetaldehyde can be reported as a summation of the reactions (A.14) and (A.20). This leads us to the overall stoichiometric expression as follows:

$$3h\nu + C_2H_4O_{(g)} + H_2O_{(l)} \xrightarrow{TiO_2-Pt} H_{2(g)} + CH_{4(g)} + CO_{2(g)} \quad (A.28)$$
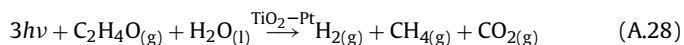
Thus, one can conclude that for the formation of two H_2 molecules requires three photons. As a result, the theoretical quantum efficiency for this step based on the $H^\bullet$ formed, is 1 as follows:

$$\varphi_{theor} = \frac{\text{moles of } H^\bullet}{\text{moles of photons}} = 0.666 \quad (A.29)$$

Appendix B. Balance of H^+ species and pH influence on hydrogen production

At time $t = 0$ with no irradiation, the $[H^+]$ and $[H^+]_{ads}^*$ are at equilibrium such as,

$$K[H^+] = [H^+]_{ads}^*$$

As soon as the lamp is turned on the following applies:

$$k_f a_v \frac{1}{\rho_{cat}} \omega V_L \{[H^+] - H^+]^*\} = k_r \omega V_L [e^-][H^+]^* + V_L \frac{d[H^+]^*}{dt} \quad (B.1)$$

With $\omega = W_{cat}/V_L$.

Thus the transport of $[H^+]$ protons through the film surrounding every single aggregate contribute to both the consumption of $[H^+]_{ads}^*$ cations and to the accumulation/de-accumulation of $[H^+]^*$ species.

$$\frac{k_f a_v W_{cat}}{\rho_{cat} V_L} \{[H^+] - [H^+]^*\} = \frac{k_r W_c}{V_L}[e^-][H^+]_{ads}^* + \frac{d[H^+]^*}{dt} \quad (B.2)$$

and

$$K \frac{d[H^+]_{ads}^*}{dt} = \frac{k_f a_v W_{cat}}{\rho_{cat} V_L} \{[H^+] - [H^+]^*\} - k_r W_c [H^+][e^-] \quad (B.3)$$

where,

$$\alpha = \frac{k_f a_v W_{cat}}{\rho_{cat} V_L}, \qquad \beta = \frac{k_r W_c K[e^-]}{V_L}$$

Thus,

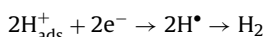$$K\frac{d[H^+]^*_{ads}}{dt} = \{\alpha[H^+] - (\alpha + \beta)[H^+]^*\} \tag{B.4}$$

In order the production of hydrogen will proceed as steady process, one should have $d[H^+]^*_{ads}/dt \approx 0$ and $[H^+]$ very close to $[H^+]^*$

To achieve this $\alpha \gg \beta$

$$\frac{\beta|_{t\to 0}}{\alpha} = \frac{k_r W_{cat} K[e^-]/V_L[H^+]}{k_f a_v W_{cat}/V_L \rho_{cat}[H^+]} \tag{B.5}$$

Considering that,

$$2H^+_{ads} + 2e^- \to 2H^\bullet \to H_2$$

Then at irradiation times approaching zero it follows,

$$\frac{\beta|_{t\to 0}}{\alpha} = \frac{2dN_{H_2}/dt|_{t=0}V_{gas\ tank}}{k_f a_v W_{cat} V_{T,Liq}/V_L \rho_{cat}[H^+]} \tag{B.6}$$

Moreover and considering that the various parameters involved in the case of our study could be estimated for 1 wt% Pt on DP25 loaded as:

$k_f = 2 \times D_{H_2}/d_p = 0.96\,\text{cm/s}$; $a_v = 6/d_p = 60{,}000\,\text{cm}^2/\text{cm}^3$; $\omega = W_{cat}/V_L = 0.00015\,\text{g/cm}^3$; $\rho_{cat} = 4.23\,\text{g/cm}^3$; and $2dN_{H_2}/dt|_{t=0} = 3.47 \times 10^{-5}\,\mu\text{moles}/(\text{cm}^3\,\text{s})$; $V_{gt} = 5716\,\text{cm}^3$; $V_{T,L} = 6000\,\text{cm}^3$ for all pH's then,

$$\frac{\beta|_{t\to 0}}{\alpha} = \frac{(3.47 \times 10^{-5}\,\mu\text{moles}/(\text{cm}^3\,\text{s}))(5716\,\text{cm}^3)}{(12{,}255\,\text{cm}^3/\text{s})[H^+](\mu\text{moles}/\text{cm}^3)}$$

$$= \frac{1.62 \times 10^{-5}\,\text{moles/L}}{[H^+](\text{moles/L})} \tag{B.7}$$

$$\frac{\beta|_{t\to 0}}{\alpha} = \frac{(1.62 \times 10^{-5})}{[H^+]} \ll 1 \tag{B.8}$$

In summary, only for the experiments at pH = 4 the condition of Eq. (B.8) is satisfied. Thus, pH = 4 is expected to yield a steady production of hydrogen $(dN_{H_2}/dt) = 0.1984\,\mu\text{moles/s}$. This is in fact what was obtained experimentally at pH = 4 using 1 wt% Pt on DP25. Other pH's however such as the pH of 7 or 10 were limited by the supply of $[H^+]$ species as is expected from (B.8).

References

[1] A. Kudo, International Journal of Hydrogen Energy 32 (2007) 2673–2678.
[2] M. Maicu, M.C. Hidalgo, G. Colon, J.A. Navio, Journal of Photochemistry and Photobiology A: Chemistry 217 (2011) 275–283.
[3] Y. Li, Y. Xie, S. Peng, G. Lu, S. Li, Chemosphere 63 (2006) 1312–1318.
[4] L. Arriaga, A. Fernandez, O. Solorza, International Journal of Hydrogen Energy 23 (1998) 995–998.
[5] H. Bahruji, M. Bowker, P.R. Davies, L.S. Al-Mazroai, A. Dickinson, J. Greaves, D. James, L. Millard, F. Pedrono, Journal of Photochemistry and Photobiology A: Chemistry 216 (2010) 115.
[6] C.A. Emilio, J.J. Testa, D. Hufschmidt, G. Colon, J.A. Navio, D.W. Bahanemann, M.I. Litter, Journal of Industrial and Engineering Chemistry 10 (2004) 129–138.
[7] T.A. Egerton, J.A. Mattinson, Journal of Photochemistry and Photobiology A: Chemistry 194 (2008) 283–289.
[8] D. Riassetto, C. Holthzinger, M. Messaoud, S. Brinche, G. Berthome, F. Roussel, L. Rapenne, M. Langlet, Journal of Photochemistry and Photobiology A: Chemistry 202 (2009) 214–220.
[9] C.M. Blount, J.L. Falconer, Applied Catalysis B: Environmental 39 (2002) (2002) 39–50.
[10] J.M. Thornton, D. Raftery, ACS Applied Materials and Interfaces 4 (2012) 2426–2431.
[11] A. Fujishima, K. Honda, Nature 238 (1972) 37–38.
[12] A. Kudo, International Journal of Hydrogen Energy 31 (2006) 197–202.
[13] H.M. Coleman, K. Chiang, R. Amal, Chemical Engineering Journal 113 (2005) 65–72.
[14] N. Castillo, L.A.G. Serrano, C.A.F. Sandoval, R. Perez, Journal of Nanotechnology 3 (2003) 199–202.
[15] K. Mogyorosi, A. Kmetyko, N. Czirbus, G. Vereb, P. Sipos, A. Dombi, Reaction Kinetics and Catalysis Letters 98 (2009) 215–225.
[16] A. Nadeem, G. Waterhouse, H. Idriss, Catalysis Today 182 (2012) 16–24.
[17] F.C. Wang, C.H. Liu, C.W. Liu, J.H. Chao, C.H. Lin, Journal of Physical Chemistry 113 (2009) 13832–13840.
[18] A. Patsoura, D.I. Kondarides, X.E. Verykios, Catalysis Today 124 (2007) 94–102.
[19] M. Zhou, Y. Li, S. Peng, G. Lu, S. Li, Catalysis Communications 18 (2012) 21–25.
[20] X.J. Zheng, L.F.Z. Wei, h. Zhang, Q.J. Jiang, Y.J. Wei, B. Xie, M.B. Wei, International Journal of Hydrogen Energy 34 (2009) 9033–9041.
[21] S. Chavadej, P. Phuaphromyod, E. Gulari, P. Rangsunvigit, T. Sreethawong, Chemical Engineering Journal 138 (2008) 489–495.
[22] M. Ikeda, Y. Kusumoto, Y. Yakushijin, S. Somekawa, P. Ngweniform, B. Ahmmad, Catalysis Communications 8 (2007) 1943–1946.
[23] C. Zhou, Z. Ren, S. Tan, Z. Ma, X. Mao, D. Dai, H. Fan, X. Yang, J. LaRue, R. Copper, A.M. Wodke, Z. Wang, Z. Li, B. Wang, J. Yang, J. Hou, Chemical Science 1 (2010) 575–580.
[24] H. de Lasa, B. Serrano, M. Salaices, Photocatalytic Reactor Engineering, Springer, New York, 2005.
[25] M. Salaices, B. Serrano, H. de Lasa, Chemical Engineering Science 59 (2004) 3–15.
[26] J. Yori, J. Parera, Applied Catalysis A: General 129 (1995) L151–L156.
[27] J. Regdbuto, Photocatalyst Preparation Science and Engineering, CRC press Taylor and Francis Group, Boca Raton, FL, 2008.
[28] Y. Ikuma, H. Bessho, International Journal of Hydrogen Energy 32 (2007) 2689–2692.
[29] M. Salaices, B. Serrano, H. de Lasa, Industrial and Engineering Chemistry Research 40 (2001) 5455–5464.
[30] B. Serrano, A. Ortiz, J. Moreira, H. de Lasa, Industrial and Engineering Chemistry Research 48 (2009) 9864–9876.
[31] Y. Cheng Liu, X. Ping Qiu, Y. Qing Huang, W. Tao Zhu, Carbon 40 (2002) 2375–2380.
[32] P. Kjellin, H. Ekstrom, G. Lindbergh, A.E.C. Palmqvist, Journal of Power Sources 168 (2007) 346–350.
[33] B. Abida, L. Chirchi, S. Baranton, T.W. Napporn, H. Kochkar, J.M. Leger, A. Ghorbel, Applied Catalysis B: Environmental 106 (2011) 609–615.
[34] S. Higashimoto, K. Takamatsu, M. Azuma, M. Kitano, M. Matsuoka, M. Anpo, Catalysis Letters 122 (2008) 33–36.
[35] L. Qiuye, L. Gongxuan, Catalysis Letters 125 (2008) 376–379.
[36] V. Subramanian, E. Wolf, V. Kamat, Journal of the American Chemical Society 126 (2004) 4943–4950.
[37] R.M. Navarro, F. del Valle, J.A. Villoria de la Mano, M.C. Alvarez-Galvan, J.L.G. Fierro, Advances in Chemical Engineering 36 (2009) 113–143.
[38] J.J. Murcia, M.C. Hidalgo, J.A. Navio, V. Vaiano, P. Ciambelli, D. Sannino, International Journal of Energy 2012 (2011) 1–9.
[39] G. Yang, Z. Yan, T. Xiaa, Applied Surface Science 258 (2012) 8704–8712.
[40] S. Kundu, J. Ciston, S.D. Senanayake, D.A. Arena, E. Fujita, D. Stacchiola, L. Barrio, R.M. Navarro, J.L.G. Fierro, J.A. Rodriguez, Journal of Physical Chemistry 116 (2012) 14062–14070.
[41] G. Colon, M. Maicu, M.C. Hidalgo, J.A. Navio, A. Kubacka, M. Fernandez-Garcia, Journal of Molecular Catalysis A: Chemical 3320 (2010) 14–18.
[42] H. Arakawa, K. Sayama, Catalysis Surveys from Japan 4 (2000) 75–80 (Baltzer Sci. Publisher BV).
[43] R. Kim, J. Chattopadhyay, J. Son, D. Pak, Korean Journal of Chemical Engineering 25 (2008) 775–779.
[44] M. Salaices, B. Serrano, H. de Lasa, Chemical Engineering Journal 90 (2002) 219–229.
[45] J. Moreira, B. Serrano, O. Aaron, H. de Lasa, Industrial and Engineering Chemistry Research 49 (2010) 10524–10534.
[46] A. Cassano, C. Martin, R. Brandy, O. Alfaro, Industrial and Engineering Chemistry Research 34 (1995) 2155–2201.
[47] M. Ni, M.K.H. Leung, D.Y.C. Leung, K. Sumathy, Renewable and Sustainable Energy Reviews 11 (2007) 401–425.
[48] I. Sadeghi, P. Arbab, M. Fathizadeh, H. Fakhraee, M. Amrollahi, Advances in Materials Science and Engineering 2012 (2012) 1–5.
[49] M. Sahu, K. Suttiponparnit, S. Suvachittanont, T. Charinpanitkul, P. Biswas, Chemical Engineering Science 66 (2011) 3482–3490.
[50] V. Tiwari, J. Yiang, V. Sethi, P. Biswas, Applied Catalysis A: General 345 (2008) 241–246.
[51] N. Wu, M.N. Lee, International Journal of Hydrogen Energy 29 (2004) (2004) 1601–1605.
[52] B. Serrano, H. de Lasa, Industrial and Engineering Chemistry Research 36 (1997) 4705–4711.
[53] D.S. Muggli, J.L. Falconer, Journal of Catalysis 237 (1999) 230–237.
[54] A. Kudo, Y. Miseki, Chemical Society Reviews 38 (2009) 253–278.